Performance and Calibration of the AXAF High Resolution Camera II: the Spectroscopic Detector

R. P. Kraft, J. H. Chappell, A. T. Kenter, K. Kobayashi, G. R. Meehan
S. S. Murray, and M. V. Zombeck
Smithsonian Astrophysical Observatory
60 Garden St., MS-31
Cambridge, MA 02138
e-mail: rkraft@cfa.harvard.edu

G. W. Fraser, J. F. Pearson, J. E. Lees, A. N. Brunton
University of Leicester
Leicester LE1 7RH, United Kingdom

M. Barbera, A. Collura, and S. Serio
Instituto e Osservatorio Astronomico G. S. Vaiana, Palermo, Italy 90134

ABSTRACT

The High Resolution Camera (HRC) is one of two focal plane detector systems that will be flown on the Advanced X-ray Astrophysics Facility (AXAF). The HRC consists of two microchannel plate (MCP) detectors: one to provide large area, high position resolution imaging and timing (HRC-I), and a second (HRC-S) to provide a readout for the AXAF Low Energy Transmission Gratings. Each detector is composed of a chevron pair of CsI coated MCPs with a crossed grid charge detector and an Al/Polyimide UV/Ion shield. In this paper, we describe the operation, performance and calibration of the spectroscopic detector. In particular, we discuss the absolute quantum efficiency calibration, the point spread function of the instrument combined with the AXAF telescope, the count rate linearity, the spatial linearity, and the internal background of the instrument. Data taken in the laboratory and at the X-ray Calibration Facility at Marshall Space Flight Center are presented.

Keywords: X-rays, microchannel plates, X-ray detectors, AXAF High Resolution Camera, X-ray spectroscopy

1 INTRODUCTION

The Advanced X-ray Astrophysics Facility (AXAF) will provide high spatial and moderate spectral resolution imaging and high resolution dispersive spectroscopy of astrophysical sources in the 0.1 to 10 keV bandpass. AXAF consists of the High Resolution Mirror Assembly (HRMA), two sets of transmission gratings, and two focal plane detectors[1]. The HRMA is composed of 4 nested, iridium coated Wolter type I mirrors, and will capable of ∼1 arcsec image resolution in orbit. High resolution spectroscopy will be performed with one of two sets of transmission gratings: the Low Energy Transmission Gratings (LETG) in the 0.1 to 1 keV bandpass[2], and the High Energy Transmission Gratings (HETG) in the 0.5 to 10 keV bandpass[3]. There are two focal plane detector systems on AXAF, the High Resolution Camera (HRC)[4] and the AXAF CCD Imaging Spectrometer (ACIS)[5]. In this paper, we will discuss the performance and calibration of the HRC-S. In particular, we present preliminary results on measurements of the effective area, point spread function, and count rate linearity of the HRMA/HRC combination, as well as the absolute quantum efficiency and detector uniformity measurements.

The HRC is composed of two microchannel plate based X-ray detectors. One is designed for large area, high spatial and temporal resolution imaging (the HRC-I), the other (HRC-S) as a readout for the LETGs. The HRC is an extension of the highly successful Einstein[6] and ROSAT HRI[7] programs, but with several significant improvements, including MCPs manufactured from low noise glass, larger MCP area, and a CsI photocathode for improved response at low energies. The HRC was developed in a collaboration by the Smithsonian Astrophysical Observatory (USA), the University of Leicester (UK), and the Instituto e Osservatorio Astronomico G. S. Vaiana (Italy).

We have performed an extensive calibration of various sub-components of the HRC at SAO, Leicester, and Palermo[8,9]. The flight instrument was shipped to Marshall Space Flight Center (MSFC) in February, 1997, where the HRC was tested and calibrated with the HRMA and gratings in the X-ray Calibration Facility (XRCF). The flight instrument was then returned to SAO to make some minor electronic modifications and perform flat field measurements. After returning to MSFC for thermal/vac testing, the instrument was shipped to Ball Aerospace in Boulder, Colorado for integration into the Science Instrument Module. It will then be taken to TRW in California to be integrated with the rest of the satellite. From there, the instrument will be shipped back to Kennedy Space Center and launched in September, 1998.

This paper is organized as follows. The HRC-S is described in section 2. The most recent calibration data is presented in section 3. Section 4 contains a brief summary and conclusion.

2 DETECTOR DESCRIPTION

The HRC-S consists of three pairs, or segments, of microchannel plates (MCPs) in a chevron configuration with Al/polyimide UV/Ion shields (UVIS)[10]. All three segments share a single modified crossed grid charge detector (CGCD) readout. A schematic diagram of the operation of the HRC is contained in Figure 1. Each segment is 30mm×100mm, and the three segments are abutted such that the detector is ∼300mm in length in the LETG disperson direction, with 1.5 mm gaps between each segment. The spectral range of the LETG and HRC-S extends to 160Å, with a dispersion of 1.15Å/mm. The center segment is aligned perpendicular to the optical axis of the telescope, while the outer two segments are tilted to more closely match the Rowland circle of the LETGs. The centerline of the detector is offset from the optical axis by 4 mm so that the gaps between the segments are not centered on the zeroth order. A schematic diagram of the arrangement of the three segments is contained in Figure 2.

The MCPs in the HRC-S were manufactured by the Phillips Corporation of Brieve, France. They have 12.5 μm diameter pores on 15 μm centers with an L/D ratio of 120:1. The pores are biased at 6 degrees in the cross-dispersion direction. The 6 degree bias maximizes the HRC QE with respect to the cone angles of the 4 shells of the HRMA. The tilt in the cross-dispersion direction minimizes QE variations in the dispersion direction due to the variation of the angle between the incident photon and the MCP pore. Decays from radio-isotopes of K and Rb were found to be the largest source of internal background in the Einstein and ROSAT HRIs. The HRC MCPs have been manufactured from a glass virtually free of these elements. The internal background of the HRC-S is 0.04 cts/(cm^2 s), a factor of 10 reduction over conventional MCPs. The HRC is also provided with active and passive shielding to reduce background in the space environment. The HRC is surrounded by a tantalum shield to block hard X-rays and gamma-rays, A five-sided anti-coincidence shield consisting of a plastic scintillator and photomultiplier tubes vetos charged particle events. The background on orbit from all

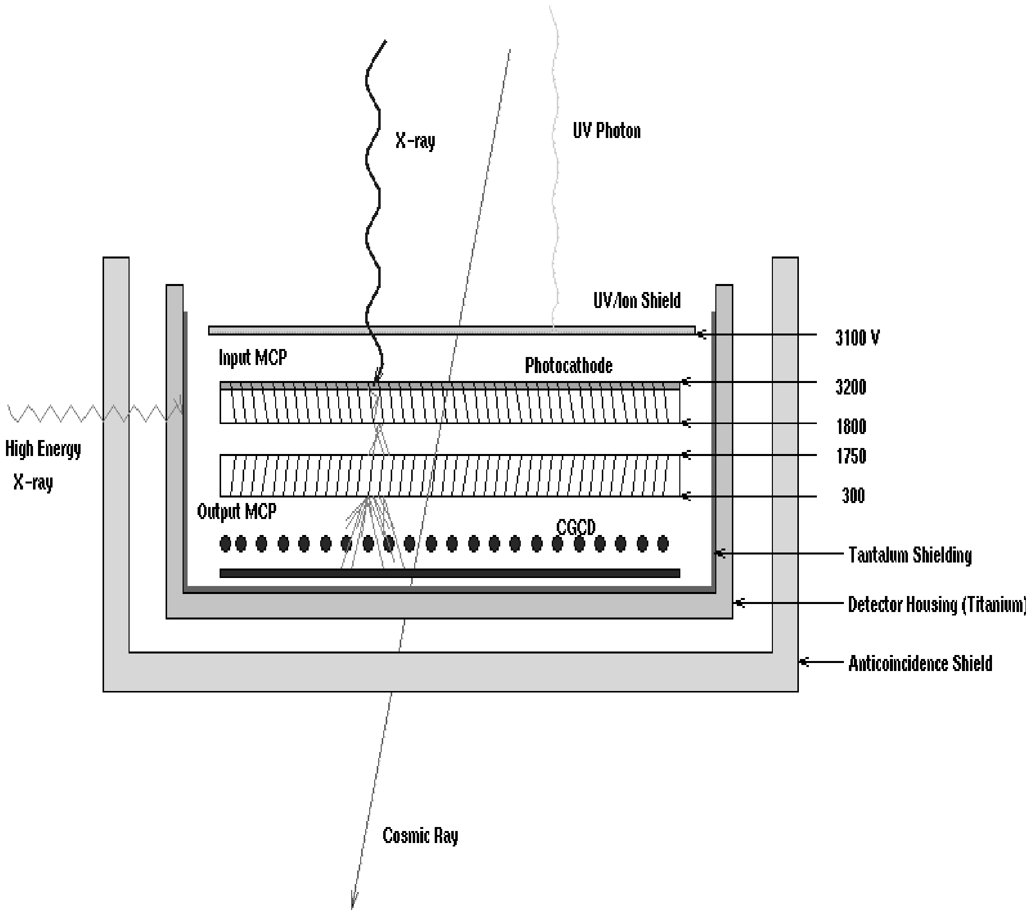

Figure 1: Functional diagram of the HRC showing the UVIS, MCPs, and modified CGCD. The tantalum shield and anti-coincidence shield are for background reduction/rejection.

sources is expected to be $\sim 4\times10^{-7}$ cts/arcsec^2/s.

The UV/Ion shields of the HRC-S are composed of aluminum and polyimide, and have a complex structure to optimize the detector for use with the LETGs[11,12]. Their primary purpose is to block ultraviolet light, low energy electrons, and ions. The shield is also necessary to eliminate the time variable background seen on MCP detectors without a shield[13]. It is grounded to prevent photoelectrons from the web between the pores creating a halo (as was seen on ROSAT). A schematic diagram of the shields (which were manufactured by Luxel Corporation) is given in Figure 3. The central shield has 2500 Å of polyimide, the two wing segments 2000 Å. Each segment also has two regions with different Al thicknesses. The central segment has a central 'T' region with 1000 Å of Al, and 300 Å elsewhere. The two wing segments have 2000 Å of Al across a thin strip, and 300 Å elsewhere. This design maximizes the soft X-ray QE at the longest wavelengths of the AXAF bandpass, but minimizes the UV flux in zero order. The thick region of Al on the wings can be used to estimate higher order contamination. The calibration of these shields is discussed elsewhere in these proceedings[11].

There is a single 300 mm $\times$ 20 mm Crossed Grid Charge Detector readout for all three segments of the HRC-S. A single readout is used to minimize the gaps between the segments, and the ends of the CGCD are tilted to match the orientation of the wing segments. The substrate of the grid was machined from a fine grained, isostatically pressed Al_2O_3 powder. Normally a CGCD is composed of wound wires (as is the case for the HRC-I). The grid in the cross-dispersion direction of the HRC-S is composed of conventionally wound Au

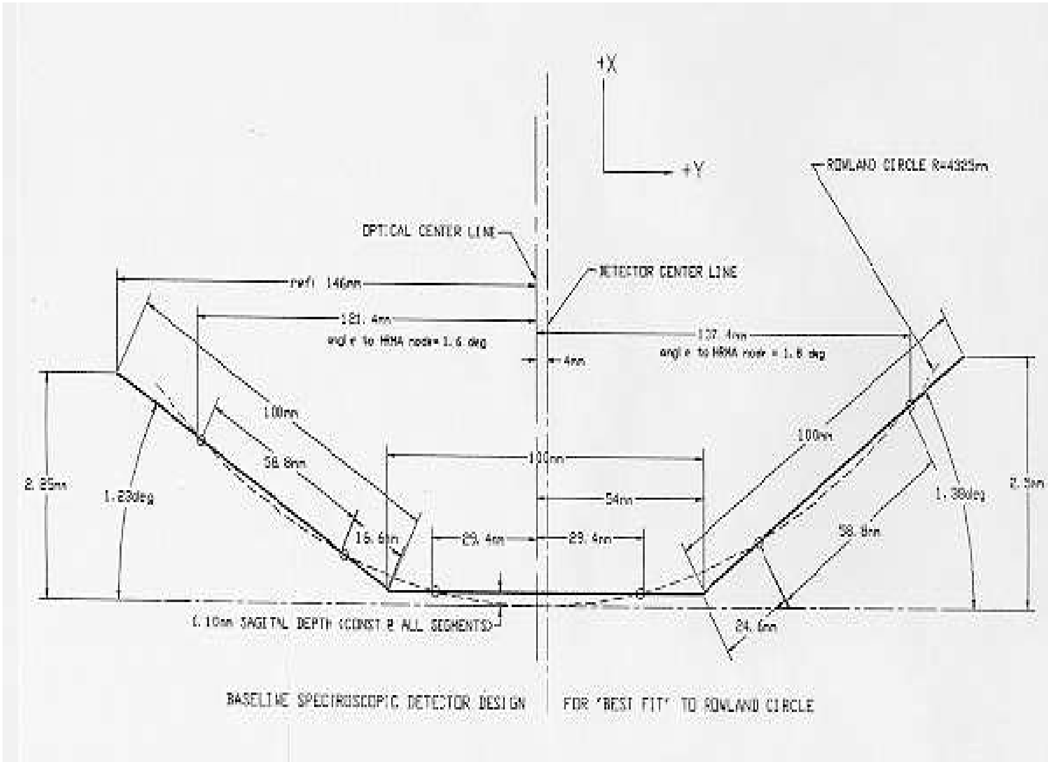

Figure 2: Schematic diagram of the layout of the three segments of the HRC-S. Note the tilt of the two wing segments relative to the center segment.

alloy wires. This is not practical along the long and tilted dispersion direction, however. As an alternative, electroplated Au strips (190 μm wide on 200 μm centers) were deposited along the dispersion direction. There is no difference in grid performance of the HRC-S and HRC-I.

Every wound wire or Au strip is tied together by a resistor (10 kΩ for the wires, 30 kΩ for the strips), and every eighth wire/strip (called a tap) is attached to a charge sensitive preamplifier for position determination. The CGCD contains 16×192 taps for the HRC-S. In order to make the HRC-S and HRC-I readouts redundant (the HRC-I has 64×64 taps) a multiplexing readout scheme is used, and every 64th tap along the dispersion axis is connected together. There is then a threefold degeneracy along the dispersion direction in the position of any event. This degeneracy is removed by determining which segment the event originated in by reading a signal from the bottom electrode of each of the three segments. In previous missions, the position of an event was determined by centroiding the charge over all preamplifiers along an axis (16 per axis on the ROSAT HRI). The cumulative noise from 64 preamplifiers would seriously degrade the position resolution of the detector. As an alternative, each event is centroided using the three taps with the largest signal on each axis[14]. The temporal resolution of the readout and associated electronics is 16 microseconds.

The HRC-S has little intrinsic energy resolution, and order sorting in astrophysical spectra will therefore be a complex problem. In an effort to overcome this, a Two Facet Reflection Filter (TFRF) was added to the original HRC-S design. The TFRF is a Cr/C coated mirror that can be inserted along the dispersion axis. Above the Cr L/C K edges, the reflectivity of the mirror is low, and it can be used to suppress the higher orders. It is estimated that the TFRF can provide an order of magnitude or more suppression of higher orders. There is a gap in the TFRF along the center of the center segment so that all high energy photons in zeroth or first order will not be reflected by the filter. The two facets are necessary to accomodate the spread of the HRMA cone angles. The TFRF is described in more detail elsewhere[10,15].

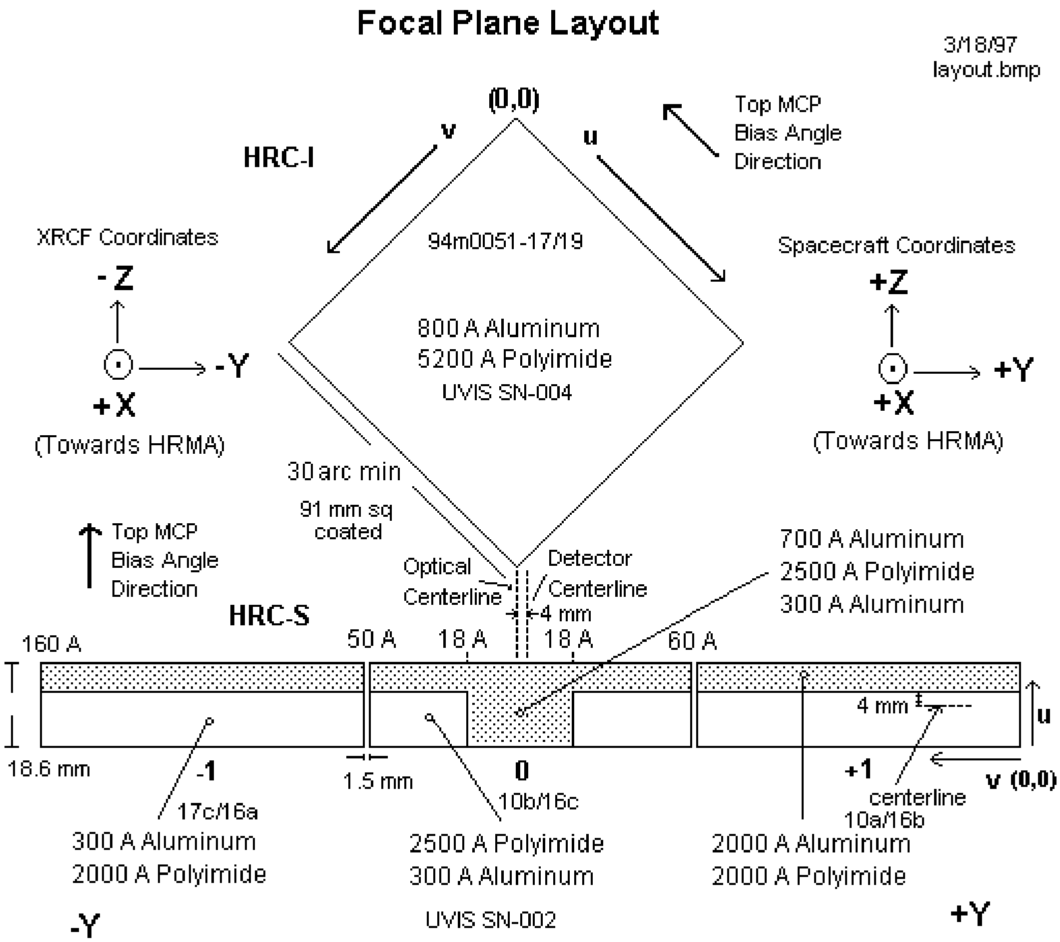

Figure 3: Schematic diagram of HRC UVIS and layout of the instrument.

3 CALIBRATION OF THE FLIGHT INSTRUMENT

A comprehensive calibration of the HRC was planned after careful consideration of the scientific goals of the mission[8,9]. The parameters of the HRC-S that must be calibrated to a high precision to meet these goals are the absolute quantum efficiency, gain, background, spatial uniformity, the spatial resolution and the count rate linearity. Our calibration plan can be divided into three distinct components: pre-delivery subassembly and full flight instrument laboratory calibration, XRCF calibration with the HRMA (and gratings), and synchrotron measurements of the quantum efficiency of CsI coated MCPs over the 0.1 to 10 keV bandpass at the Daresbury Synchrotron Radiation Source. Our plan was to perform extensive flat field measurements of the flight instrument at SAO at several discrete energies and angles of incidence before delivery to the XRCF. The synchrotron measurements provides the absolute QE of the instrument between the discrete energies measured in the lab and the detailed edge structure in the photocathode. At XRCF, we would measure/confirm the QE and spatial uniformity at a few points, and measure the point spread function and count rate linearity with the HRMA. We would also measure the QE and energy resolution of the HRMA/LETG/HRC-S combination at the XRCF.

Because of scheduling constraints, only part of this laboratory calibration was carried out before delivery to Marshall Space Flight Center. At the XRCF calibration, two problems with the flight instrument were discovered. First, the MCP gain was larger than expected. The reason for this is unknown. The gain of the preamplifiers was preset in hardware to correspond to a lower MCP gain. Because of this, ~50% of the events were saturating the pulse-height electronics and confusing the positioning algorithm. The MCP high voltage had to be turned down to restore the image quality. At this lower gain, the detector exhibited large QE and gain non-uniformities. Second, there was a 91 kHz ripple on the high voltage power supply which was coupled into the output electronics. This was particularly severe for the HRC-S because of the multiplexed output scheme. It was necessary to increase the lower level threshold to eliminate electronic noise. As a result, many 'real' X-ray events were also eliminated.

The instrument was returned to SAO after the XRCF calibration to correct these problems. The signal into the preamplifiers was reduced by installing resistive dividers, and the 91 kHz HV ripple was eliminated with an RC filter. A series of flat field measurements were made at SAO before and after the modifications to transfer the XRCF calibration to the current configuration. These changes and the calibration transfer are discussed in detail elsewhere[16]. In this section, we will discuss preliminary results of the post fix flat field measurements and the XRCF calibrations of the HRC-S (the synchrotron data have been presented previously[8,17]).

4 LABORATORY FLAT FIELD MEASUREMENTS

Flat fields of the HRC-S were made to measure the absolute quantum efficiency and detector uniformity. A schematic diagram of the experimental setup is given in Figure 4. The HRC-S was attached to a vacuum pipe by a mechanical snout which ensured that only one segment was illuminated at any time, and the TFRF was blocked by a mechanical paddle. X-rays were generated by a multi-anode electron impact source. Beam filters were inserted at the source to reduce the flux (typically ~ 1200 cts/s in the HRC) and remove continuum contamination. The central segment was calibrated at 8 energies, and each of the wing segments at 4. A summary of the anodes, filters, and predicted line-to-continuum ratios[8] is given in Table 1. Measurements were also made of the reflectivity of the TFRF by illuminating the flat and blocking the direct beam onto the detector with a mechanical paddle. Results of these measurements will be presented in a future publication.

Line	Energy	Filter	MFPs	V_A	L/C	Seg
B K_α	183 eV	7 μm parylene-C	5.87	600 V	48.4	-1,0,+1
C K_α	277 eV	33 μm polypropylene	5.94	1000 V	171	-1,0,+1
O K_α	525 eV	2 μm Cr	4.67	1000 V	29.3	-1,0,+1
Ni L_α	851 eV	2 μm Cu	3.80	2500 V	2.55	0
Al K_α	1487 eV	50 μm Al	5.40	4000 V	38.9	-1,0,+1
Ag L_α	2984 eV	10 μm Ag	4.86	6000 V	0.60	0
Ti K_α	4511 eV	150 μm Ti	6.80	10000 V	6.73	0
Fe K_α	6404 eV	125 μm Fe	6.97	10000 V	1.78	0

Table 1: Summary of line energies, filters, thicknesses, anode voltages, and predicted line-to-continuum ratio of the X-ray source for HRC-S flat fields.

Two proportional counters were used for absolute normalization of the beam. A beam normalization detector (BND) could be inserted (or withdrawn) via a vacuum feedthrough directly between the X-ray source and the HRC. The BND and the HRC were never run simultaneously because of the proximity of the two detectors and a slow gas leak through the thin BND window. A monitor detector (MD) was placed at 90 degrees to the beam to monitor temporal variations. The take-off angle between the electron impact source and either proportional counter was 45 degrees, so the intensity at either detector should be the same (we do not rely on this, however). Our calibration technique was to simultaneously illuminate the BND and MD to make an absolute measurement of the X-ray intensity and cross-calibrate the two proportional counters. The HRC and MD were then illuminated.

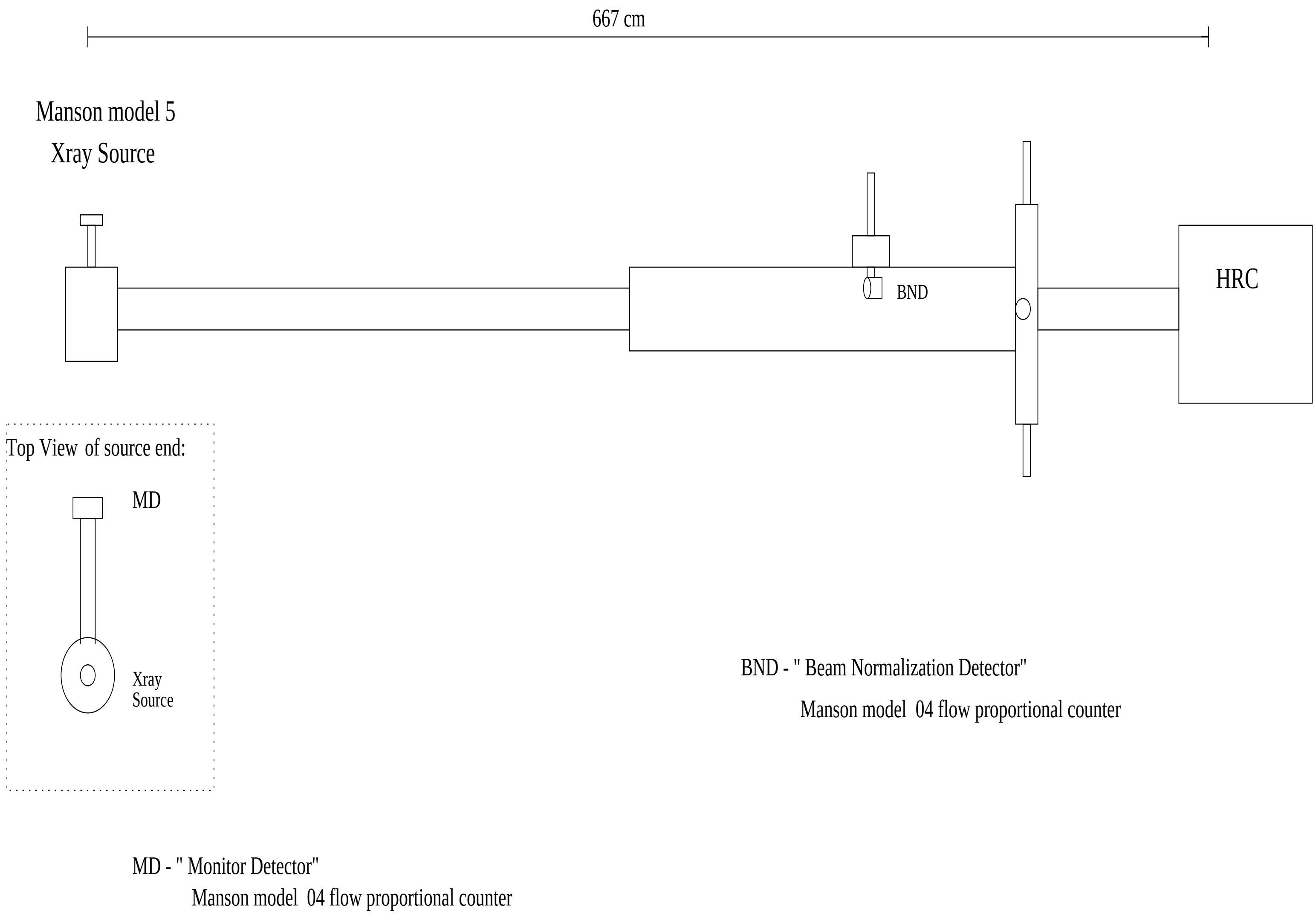

Figure 4: Schematic diagram of experimental setup for HRC flat field measurements.

Surface plots and projections of the flat fields at Al K_α for segments 0, -1, and +1 are shown in Figures 5, 6, and 7, respectively. The flat fields are similar at other energies (excepting for the UVIS structure at low energies). There is a small (~10%) gradient in the QE across the dispersion direction of all three segments. This gradient is present at all energies. We are investigating the possibility that there is some spatial non-uniformity of the X-ray beam in our experimental setup. Such a non-uniformity has not been seen in thousands of hours of previous use of the facility, however. This structure is not mimicked in the HRC-I (which was measured with the identical setup). Additionally, segment +1 has a region of slightly lower gain and QE.

The absolute QE of a given region of the detector is given by

$$Q_{HRC} = \frac{R_{HRC}}{I_{HRC}\Omega_{HRC}},$$

where R_{HRC} is the rate (cts/s) in the HRC, I_{HRC} is the x-ray intensity (phot/s sr) at the HRC, and Ω_{HRC} is the solid angle subtended by the region. The absolute intensity, I_{HRC}, is determined from the BND and MD rates, and is given by

$$I_{HRC} = \frac{R^{CC}_{BND}}{Q_{BND}\Omega_{BND}} \times \frac{R_{MD}}{R^{CC}_{MD}},$$

where R^{CC}_{BND} and R^{CC}_{MD} are the BND and MD rates measured in the cross-calibration, Q_{BND} is the calculated BND quantum efficiency, Ω_{BND} is the solid angle subtended by the BND, and R_{MD} is the MD rate during the HRC integration. The absolute QE of various regions within each of the three segments is shown in Figures 8, 9, and 10. Systematic errors will dominate these QE measurements (the statistical errorbars are smaller than the data points). The largest sources of systematic uncertainty are the QE of the BND and the spectral purity of the source. The derived MCP QE's (dividing out the transmission of the UVIS) are slightly lower (~10%) than our screening measurements made using laboratory electronics, and slightly lower (~10%) than the HRC-I QE's at the lowest energy.

5 XRCF CALIBRATION

The HRC-S was tested and calibrated in the spring of 1997 with the HRMA and gratings at the X-ray Calibration Facility (XRCF) at Marshall Space Flight Center[18]. This facility was designed to meet the unprecedented level of calibration required for AXAF. A schematic diagram of the XRCF is contained in Figure 11. The XRCF consists of three buildings and a long (518 m) vacuum pipe. One building houses three X-ray sources. A second contains two beam monitor detectors (a gas flow proportional counter and a solid state detector). The proportional counter is mounted on a stage to map out the X-ray beam across the HRMA. The third building contains the instrument chamber and control rooms. The telescope, gratings, and detectors were mounted in the instrument chamber for testing. Four proportional counters (the BND-H counters) were placed symmetrically around the front of the HRMA to continuously monitor the X-ray flux and beam uniformity at the telescope.

Four different X-ray sources/monochromators were used to generate X-rays over the AXAF bandpass. An electron impact source (EIPS) was used to generate characteristic lines from a variety of anodes (26 different anodes were available). Each anode also had filters that could be used to reduce the flux to acceptable levels and reduce continuum (bremsstrahlung) contamination. A gold coated reflection grating (HIREFS) and a W rotating anode source were used to generate monochromatic X-rays between 200 eV and 2000 eV. Higher order contamination and beam non-uniformity (up to a factor of 2 across the HRMA) make interpretation of this data difficult. Four different double crystal monochromators (DCM) were available to provide spectrally pure X-rays above 1.5 keV (in conjunction with the W rotating anode source). The beam uniformity of this source was good (about 10% across the HRMA), and higher orders contributed only a few percent of the flux. A gas discharge Penning source was used to generate soft X-ray and EUV lines from ionized Ar and Al.

XRCF measurements were made of the effective area (with and without the LETG), the count rate linearity, the point spread function, and the energy resolution of the HRC-S/HRMA and HRC-S/LETG/HRMA combinations. Over 1000 different measurements were made using the HRC-I or HRC-S. In this section, we present

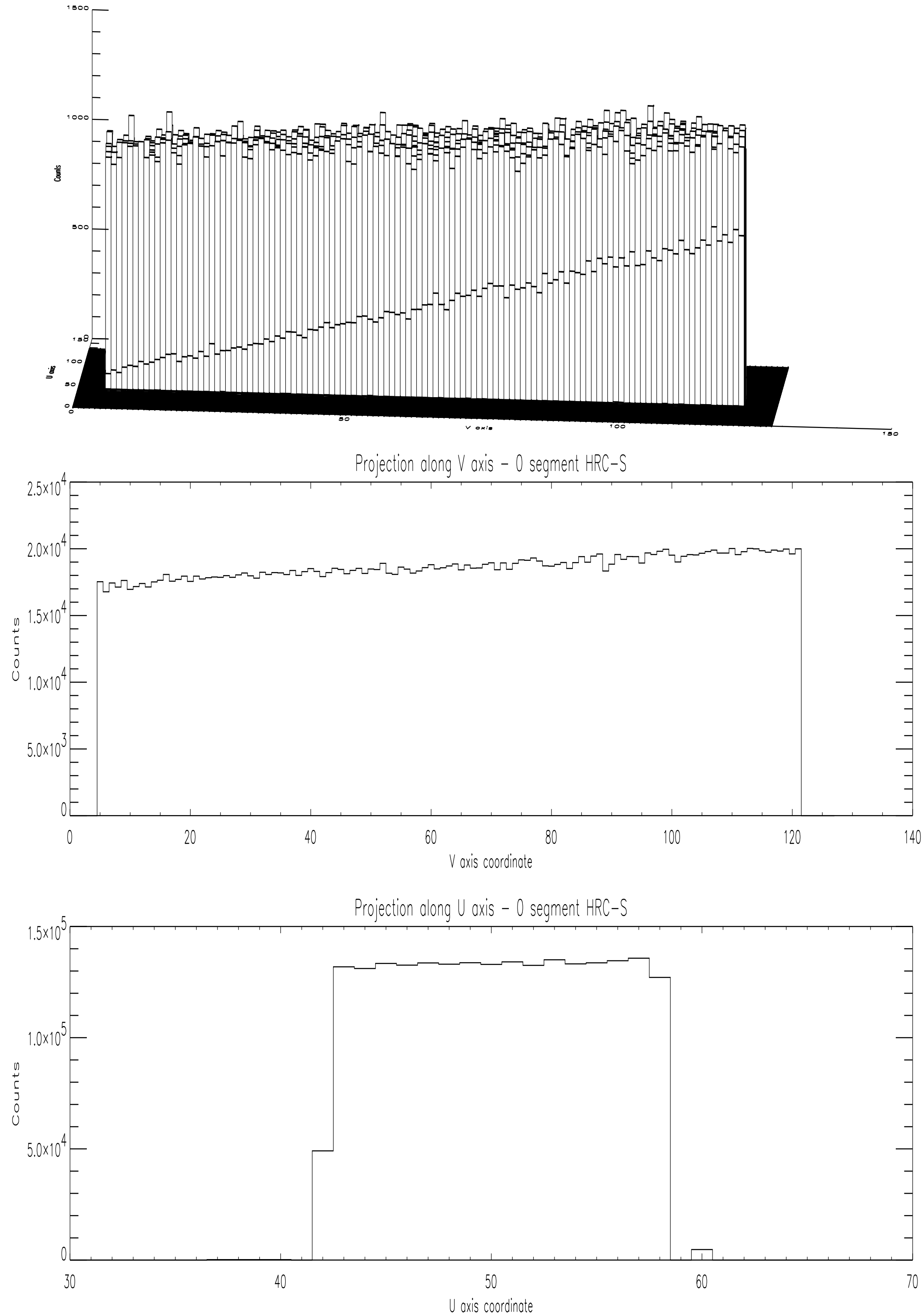

Figure 5: Surface plot and projections along the U and V axes of HRC-S segment 0, Al K_{α}. Each pixel is 0.82 mm.

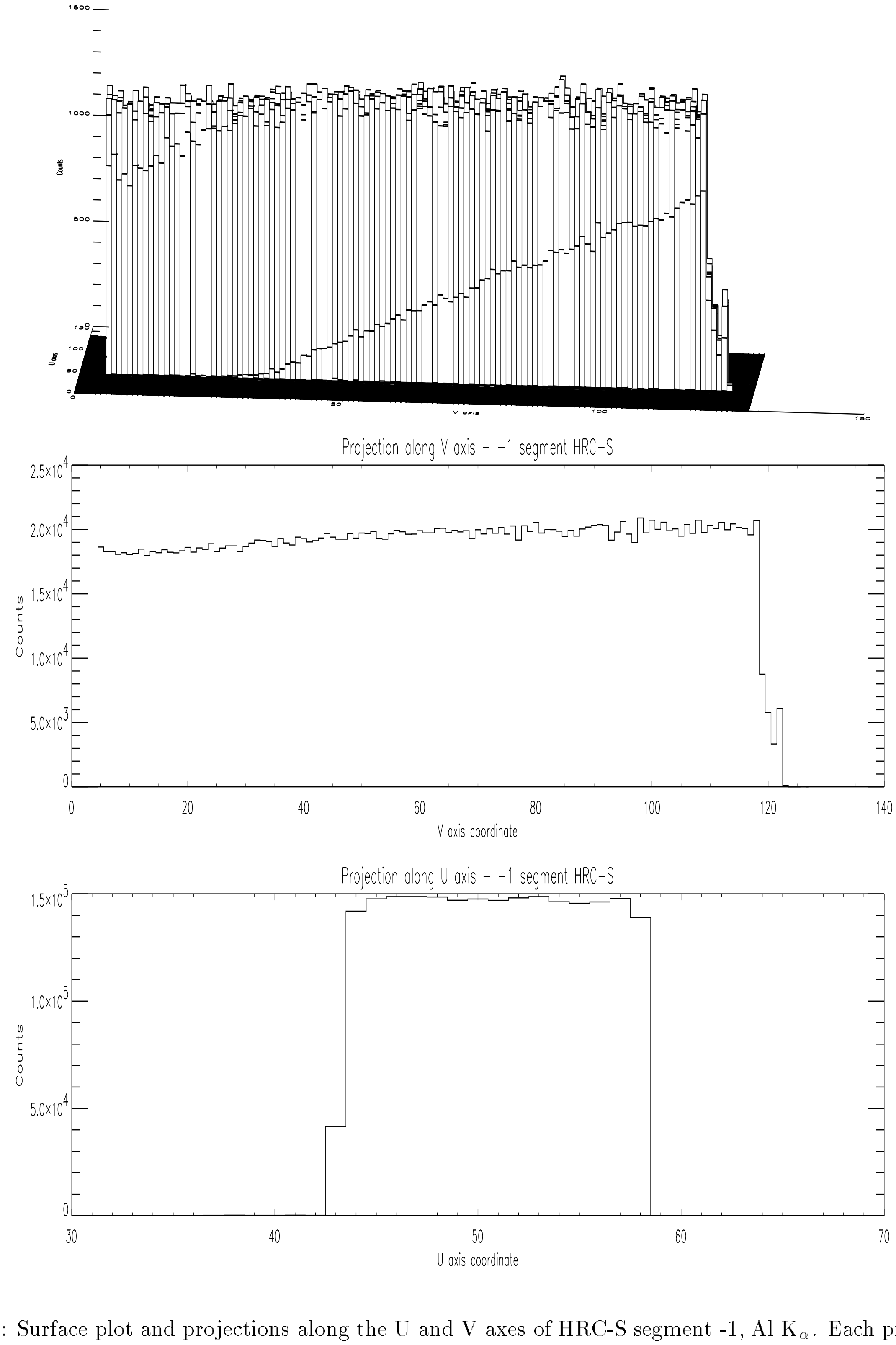

Figure 6: Surface plot and projections along the U and V axes of HRC-S segment -1, Al K_{α}. Each pixel is 0.82 mm.

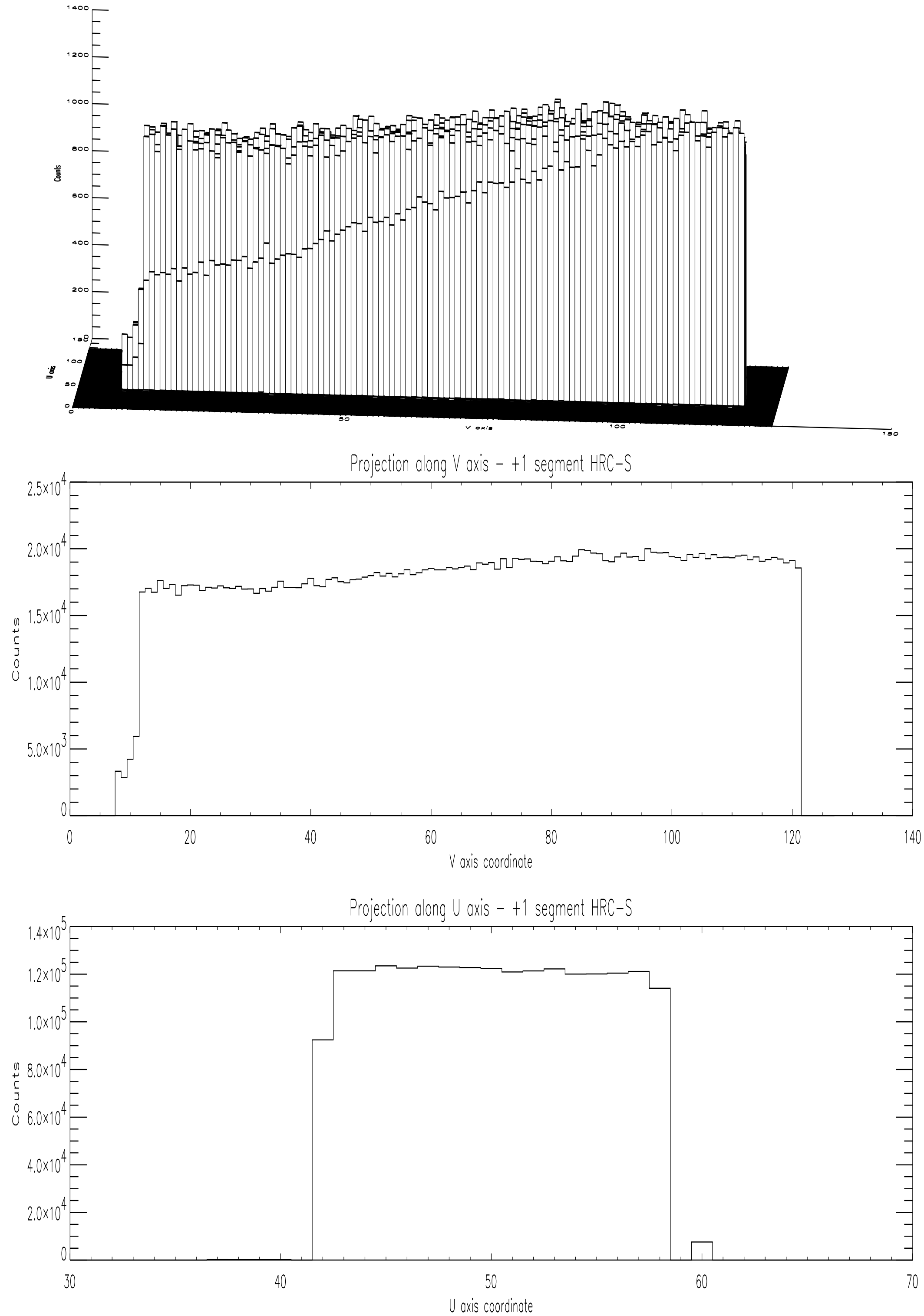

Figure 7: Surface plot and projections along U and V axis of HRC-S segment +1, Al K_α. Each pixel is 0.82 mm.

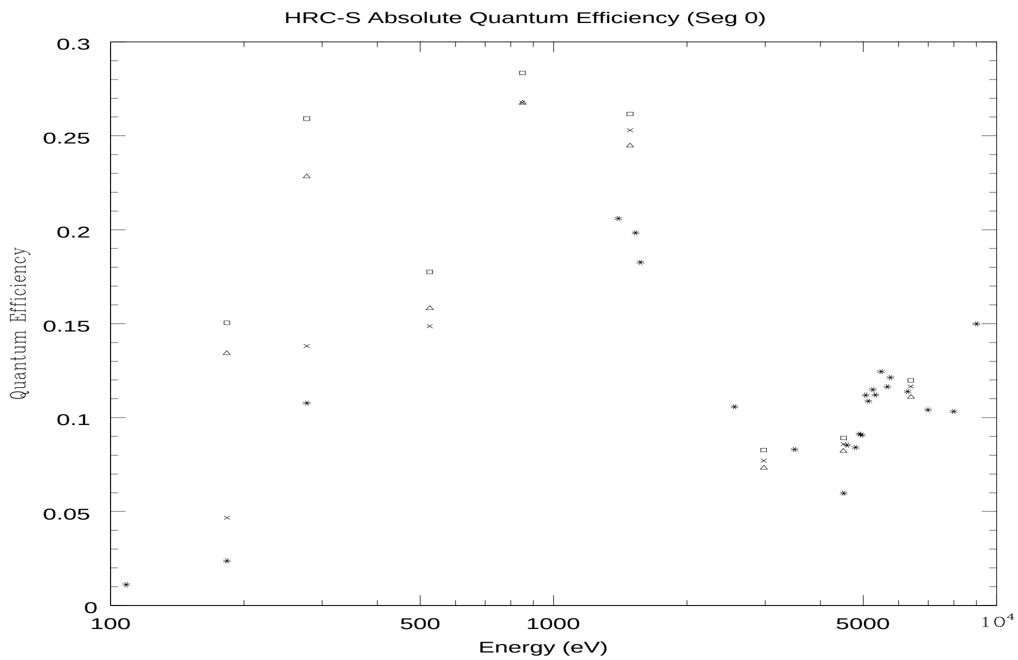

Figure 8: Absolute QE of HRC-S segment 0. The different symbols represent different regions of the detector: the cross is a central region under the thick Al, the open triangle and the open square are regions under the thin Al to the left (lower V coordinate) and right (higher V coordinate) of the central T region. The stars are the HRC-S QE derived from the XRCF data.

preliminary results from calibrations of the HRC-S/HRMA, and briefly discuss the HRC-S/LETG/HRMA calibrations. Measurements of the position (relative to the HRC-S and HRMA) and reflectivity of the TFRF were also made, and will be discussed in a future publication.

5.1 Effective Area

We have made effective area measurements with the LETG+HRC-S and with the HRC-S alone at various energies and angles of incidence. The effective area was measured by simultaneously illuminating the HRMA/HRC-S and the four BND-H proportional counters with X-rays from the EIPS, DCM, or HIREFS. The telescope was defocused for all effective area measurements to avoid extracting a large amount of charge from a small region. As above, the BNDs are used as absolute detectors. The effective area of the HRMA/HRC-S combination for data taken using the EIPS or DCM sources is then given by

$$A(E)_{EFF} = R_{HRCS} \times \frac{Q(E)_{BND} A_{BND}}{\bar{R}_{BND}} \times \frac{d^2_{HRMA}}{d^2_{BND}},$$

where $A(E)_{EFF}$ is the effective area of the HRMA/HRC-S at energy E, R_{HRCS} is the rate (cts/s) in the HRC-S, $Q(E)_{BND}$ is the calculated quantum efficiency of the BND, A_{BND} is the geometric area of the BNDs, $\bar{R}_{BND}$ is the average rate in the four BNDs, and d_{HRMA} and d_{BND} are the distances between the source and HRMA or BND, respectively. We have assumed that the four BNDs are identical. The BND-H rates are computed by taking a region of interest around the main (and escape) peak, and subtracting and appropriate background. A plot of the effective area on axis is contained in Figure 12. The errorbars in the plot are statistical only. Note the complex structure around the Cs and I L edges at $\sim$5 keV. This structure is similar to that seen in the detailed synchrotron calibrations around these edges[17]. The effective area of the HRC-I at the same energies

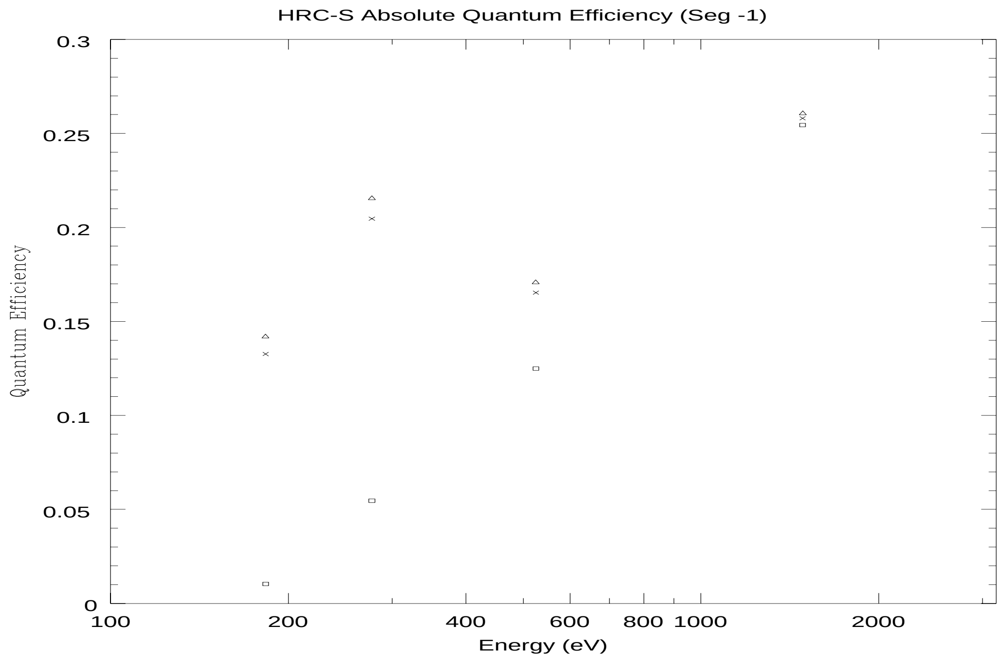

Figure 9: Absolute QE of HRC-S segment -1. The different symbols represent different regions of the detector: the open square is a region across the top under the thick Al, the cross and the open triangle are left (lower V coordinate) and right (higher V coordinate) regions under the thin Al.

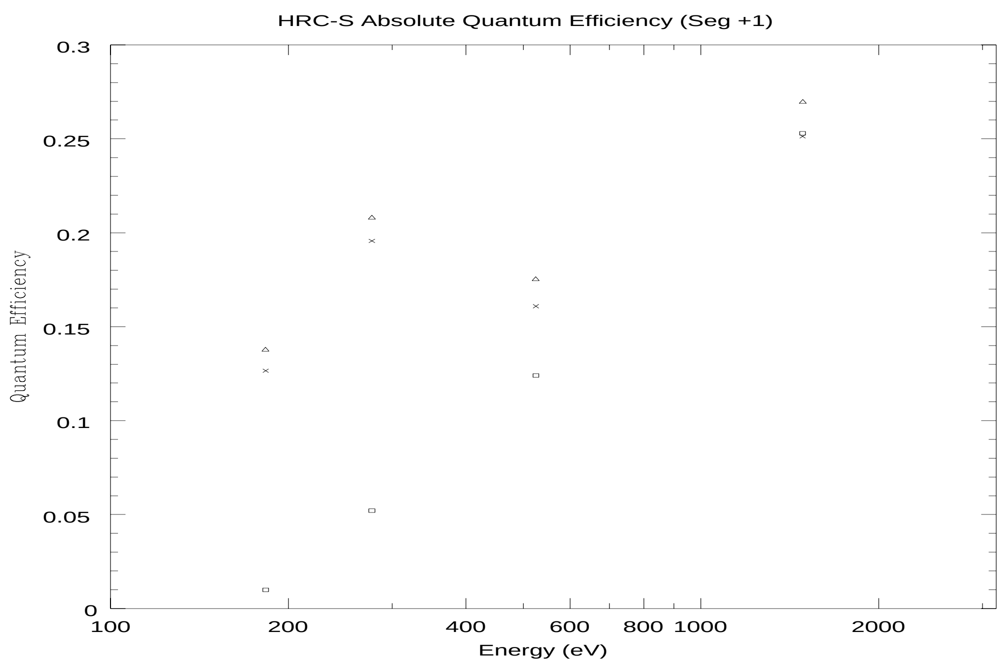

Figure 10: Absolute QE of HRC-S segment +1. The different symbols represent different regions of the detector: the open square is a region across the top under the thick Al, the cross and the open triangle are left (lower V coordinate) and right (higher V coordinate) regions under the thin Al.

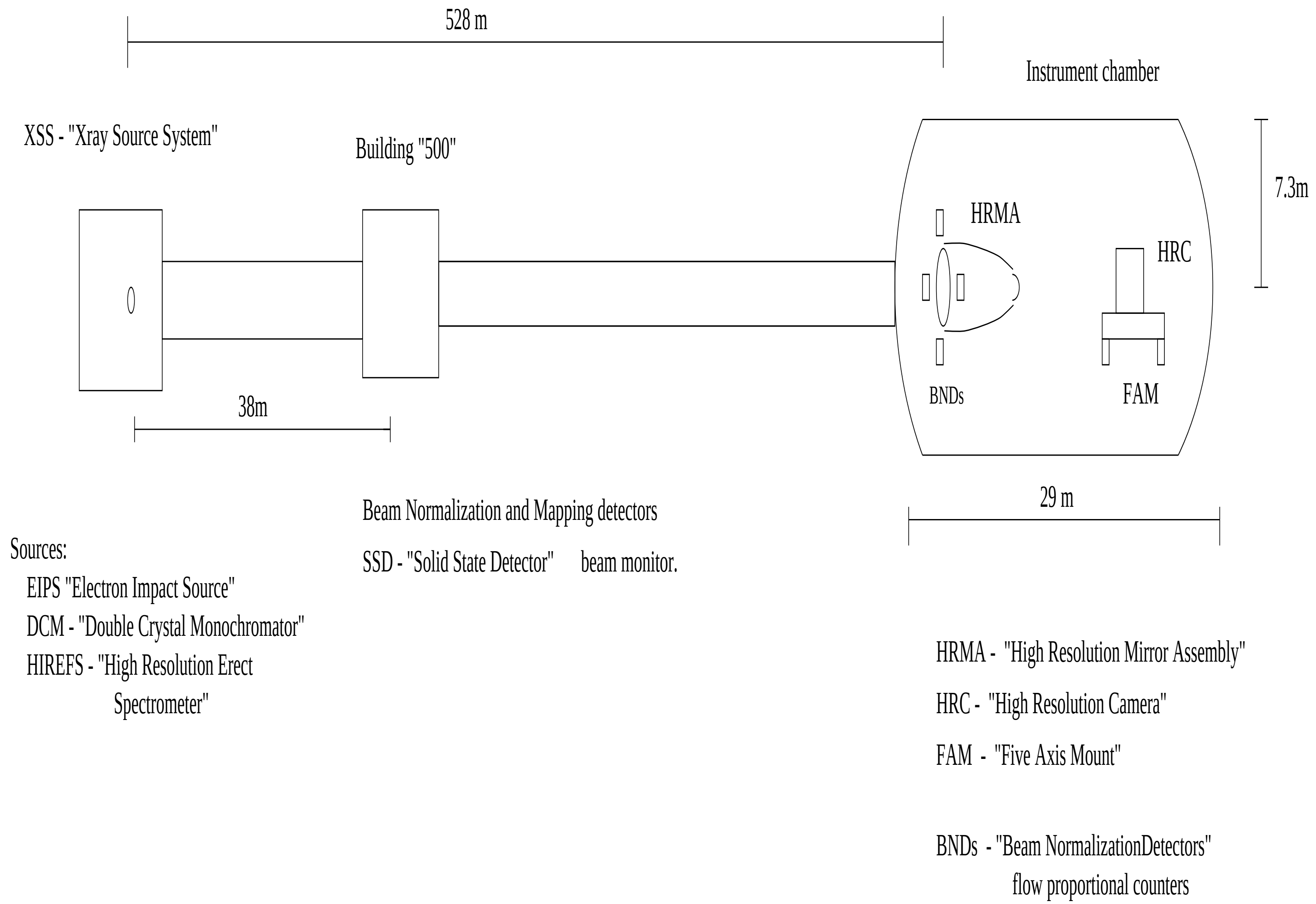

Figure 11: Schematic diagram of the X-ray Calibration Facility.

has also been plotted. Note the large difference between the detector response. This difference has been largely corrected by making a few electrical changes (see above).

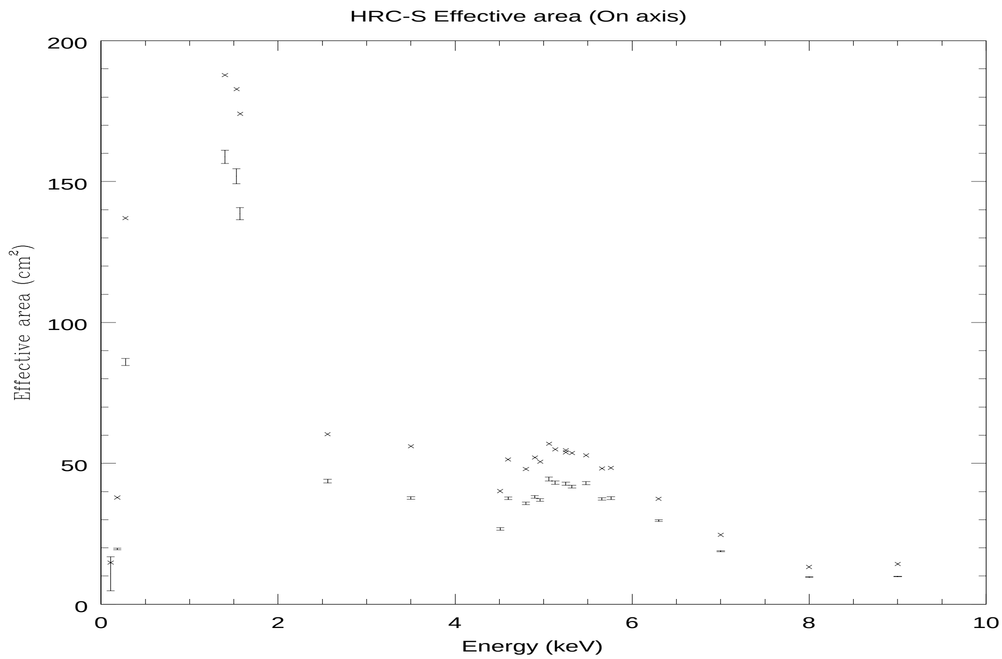

Figure 12: Effective area of the HRMA/HRC-S on axis

In the above analysis, we have assumed that the X-ray beam is nearly monochromatic and spatially uniform (or at least well described by the average of the rates in the four BND-H detectors). This is a good approximation for the DCM data and the EIPS data (C, B, and Be anodes) that we have included in the plot. Neither of these are good assumptions for the HIREFS data, however, and unfortunately the HIREFS source covers the most astrophysically interesting region of the LETG/HRC-S bandpass. Below 1 keV, higher orders contribute significantly (or dominate) the source spectrum. A BND pulse height spectrum at 392 eV is shown in Figure 13. At least 4 orders are present in this spectrum (the reflectivity of the grating is small above $\sim$ 2 keV because of the gold coating), and disentangling them in the HRC-S images requires spectral fitting of the BND pulse height data (via non-linear regression)[19], and measurements of the HRC-S QE at all higher orders. An LETG measurement was made at every HIREFS setting to help us to understand the underlying spectrum, but order separation is still a complex issue.

5.2 HRC-S + LETG performance

A series of effective area measurements were also made with the HRC-S and LETG. As a typical example, the HRC-S + LETG spectrum of the EIPS with the Ti anode and Ti filter is shown in Figure 14. The Ti L_α and L_η lines can clearly be seen, as well as continuum and C K_α contamination. The width of the Ti L_α line (27.4 Å) is in this spectrum is $\sim$0.72 Å(11.9 eV), and is the intrinsic width of the line. The resolution of the grating is much higher (more than 1000 at the longest wavelengths). A more detailed discussion of the LETG effective area and energy resolution measurements is given elsewhere[20,21].

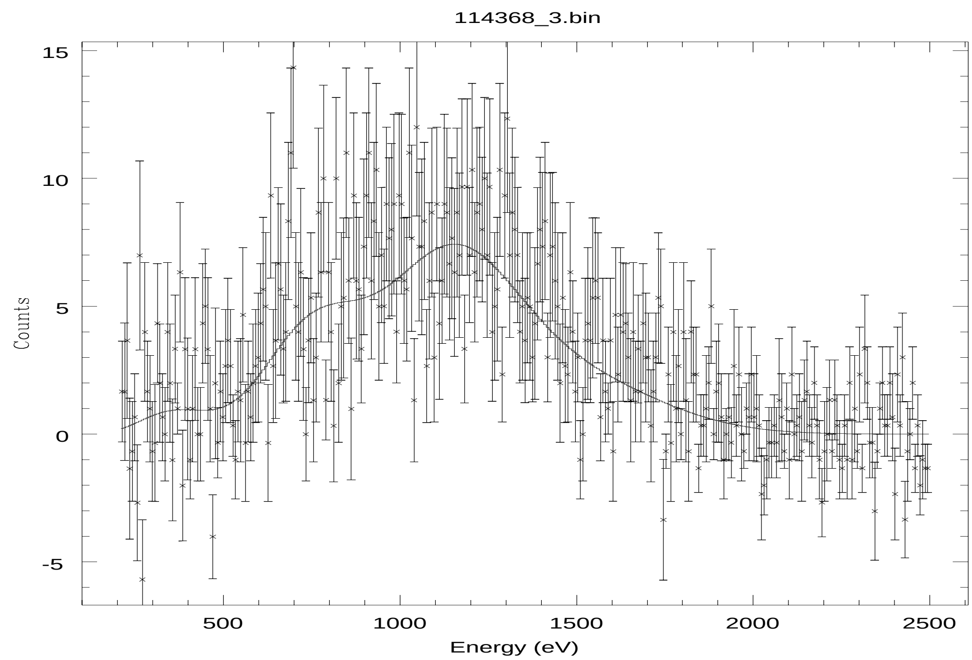

Figure 13: One BND-H spectrum of the HIREFS source (points) and best fit spectral model (histogram).

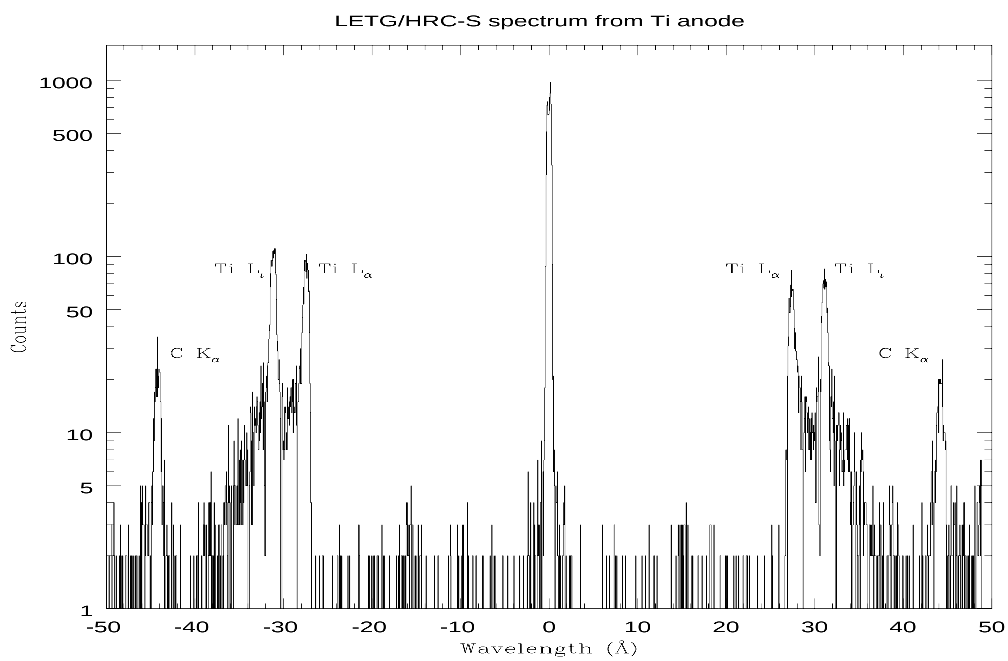

Figure 14: LETG/HRC-S spectrum of Ti anode with Ti filter. This plot is a projection of the HRC-S image along the dispersion direction.

5.3 Count Rate Linearity

Microchannel plates typically show considerable count rate non-linearities at high fluxes because of local charge extraction. The MCP has a finite recharge time after an event occurs, and if the rate is large enough, the local gain can drop so that events are lost below the lower level discriminator. The HRC-S count rate linearity (CRL) was determined simply by measuring the detector rate versus the BND-H rate as the source flux was stepped up. The BND-H rate is proportional to the incident flux, and should be linear to at least a few thousand counts per second. The telescope was in focus, and illuminated a region near the edge of the detector to avoid extracting a large amount of charge from a central region. A plot of the HRC-S rate versus one of the BND-H rates is shown in Figure 15 (both rates have been background subtracted). As can be seen from the figure, there is some marginal evidence for non-linearity at about 15 cts/s. We have made linear fits to this data, and the statistical significance of this is low. We conclude that HRC-S is approximately linear at rates of 30 cts/s or less.

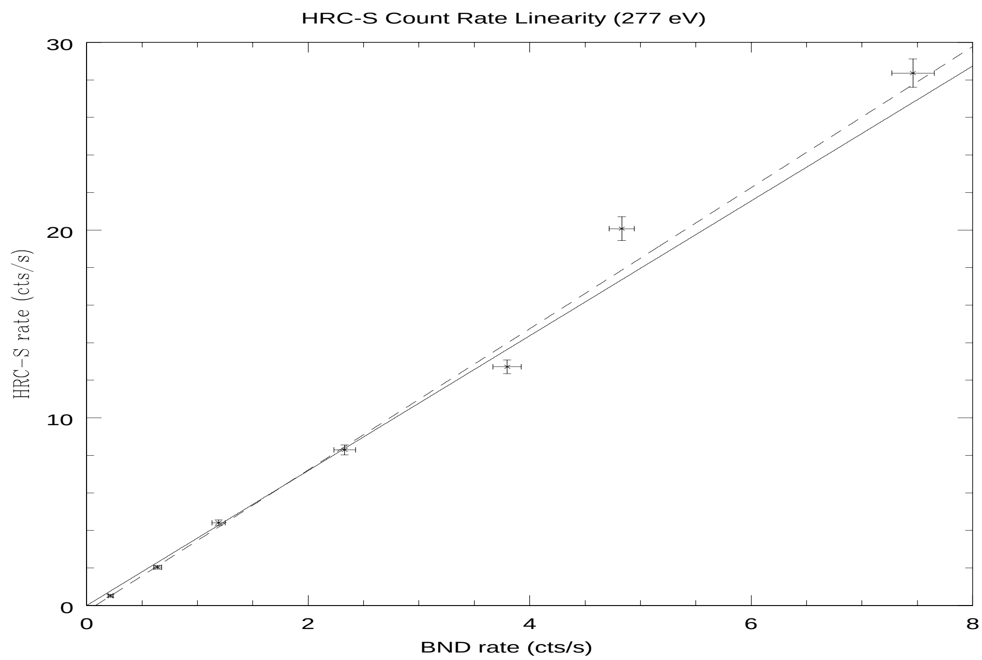

Figure 15: Count rate linearity of the HRC-S at 277 eV. The solid line is the best fit line if the fit is forced through the origin. The dashed line is the best fit line if the fit is not forced through the origin.

5.4 Point Spread Function

The point spread function (PSF) of the HRMA+HRC-S was measured at several energies at the XRCF. The telescope was in focus, and the HRC-S was moved in a serpentine pattern to avoid a large amount of charge from being extracted from a small region. We are working to remove the effect of this serpentine motion on the images. As a preliminary analysis, we have used data from the count rate linearity measurements described above to estimate the PSF. These measurements were made with the telescope in focus and the detector undithered. A surface plot of the sum of the images taken for the CRL measurements described above (E=277 eV) is contained in Figure 16. Gaussians were fit to slices of the data along the U and V axes. The width (FWHM) of the PSF in the central 135 μm of the image is 42.95 μm in the U axis and 45.85 μm in the V axis (approximately 1 arcsec angular resolution). These data slices and best fit Gaussians for each axis are plotted in Figure 17. As an alternative, the encircled energy as a function of radius is plotted in Figure 18. The half power radius is 25.72 μm.

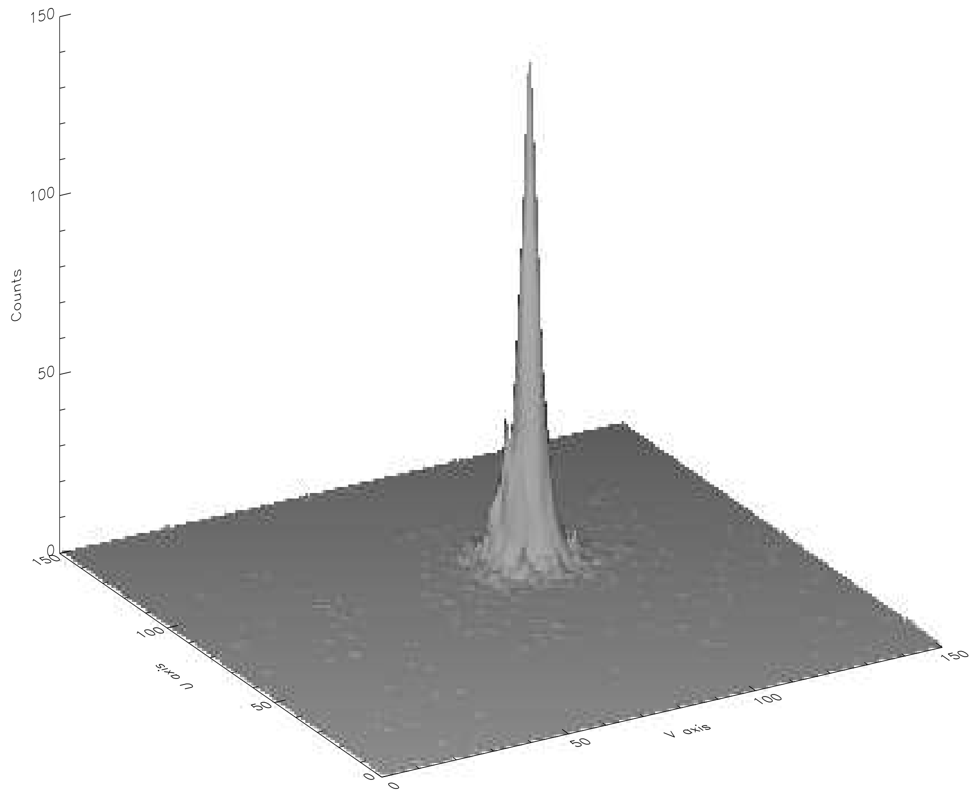

Figure 16: Point spread function of the HRC-S and HRMA

6 UV/OPTICAL SENSITIVITY MEASUREMENTS

We have measured the optical and UV sensitivity of the HRC-S wing segments. These segments have the thinnest Al and polyimide, and will therefore have the largest UV/optical sensitivity. The UV sensitivity was measured using a filtered mercury lamp (2537 Å), and the optical response with a filtered tungsten-halogen lamp (4500 Å). The absolute intensities of these lamps were measured to within 10% using a NIST calibrated photodiode. A model of the predicted HRC-S UV/optical response (UVIS transmission times CsI coated MCP response) is contained in Figure 19. The UVIS transmission was determined from a combination of laboratory measurements and a calculation using published optical constants. The CsI coated MCP response was estimated using previously published results. Also plotted is the maximum acceptable (HRC specification) UV/optical sensitivity of the flight instrument. Note that the y axis of the plot covers 10 decades in response. The uncertainties in these models are fairly large. As can be seen from Figure 19, the measured 2537 Åsensitivity agrees surprisingly well with the prediction. The optical measurement only provided an upper limit that is orders of magnitude below the prediction. The modeled optical sensitivity of the CsI MCP depends heavily on one previous (unpublished) measurement made at SAO. The bandgap of CsI is ~6.2 eV (2000 Å), and it would be reasonable to expect that the sensitivity drops rapidly beyond this wavelength. We will continue to study this issue by measuring the UV/optical sensitivity of backup HRC MCPs and UVISs.

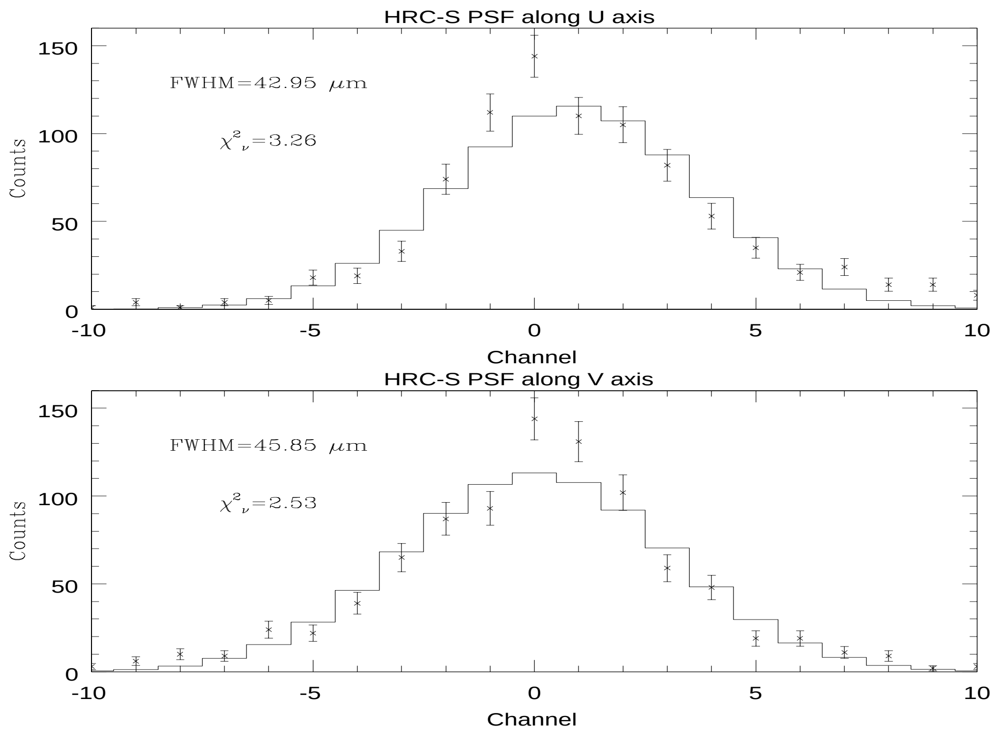

Figure 17: Best fit Gaussians to slices of the PSF along the U and V axes.

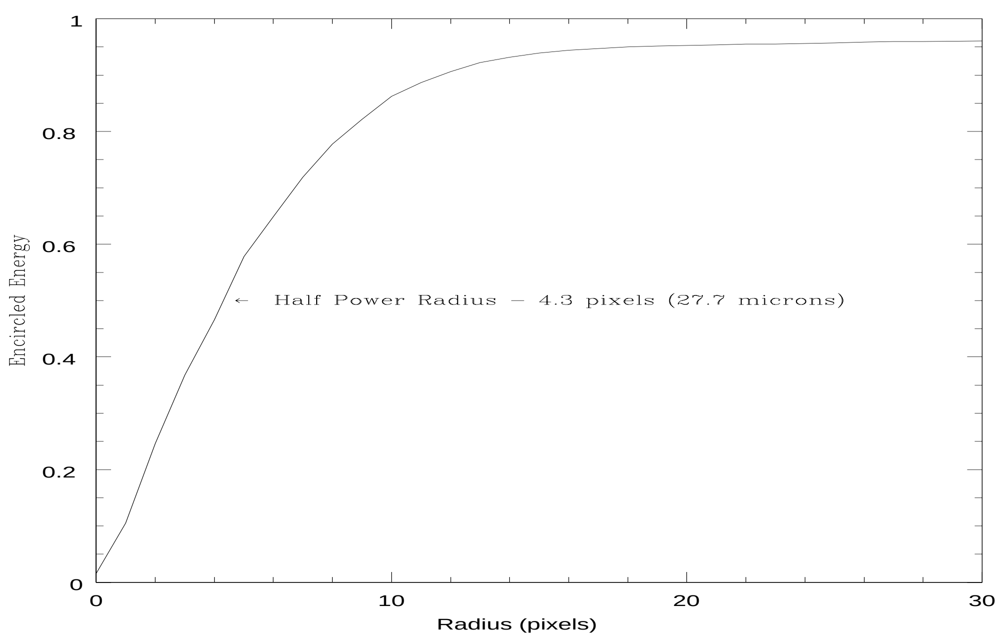

Figure 18: Encircled energy versus radius of the HRC-S/HRMA in focus at 277 eV.

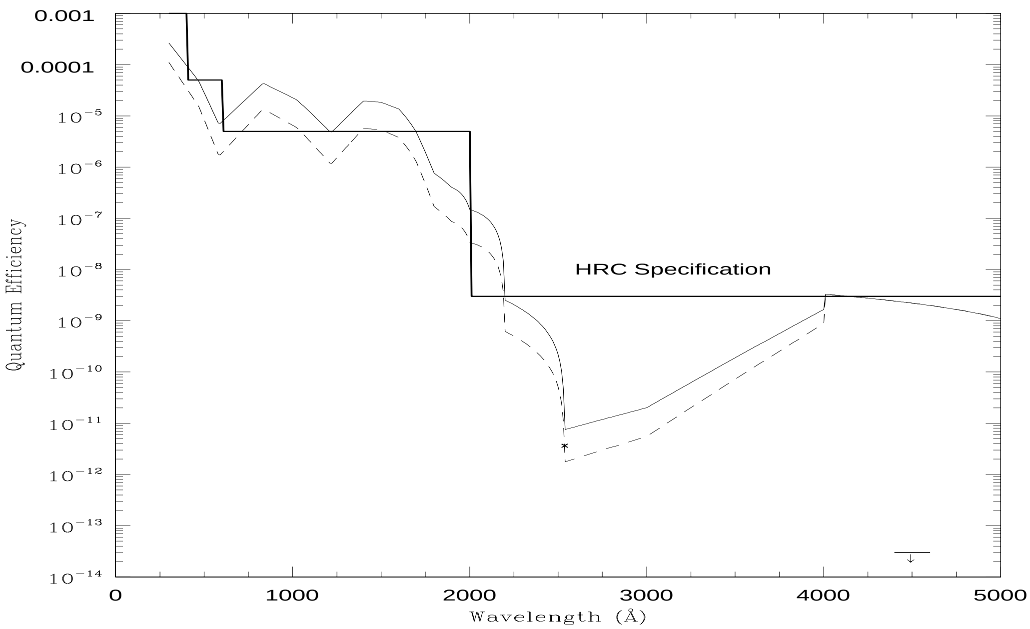

Figure 19: The calculated UV/optical QE of the wing segments of the HRC-S (the thin solid line) versus wavelength. The dashed line is the predicted QE for the nominal UVIS thickness plus the 2 sigma uncertainty. The measured values at 2537 Åand 4500 Å(an upper limit only) are also plotted. The dark solid line is the maximum UV/optical sensitivity specification. Note the logarithmic scale of the Quantum Efficiency axis.

7 SUMMARY AND CONCLUSION

We have presented preliminary results of the HRC-S calibration at XRCF, including the effective area, count rate linearity, and point spread function. The imaging performance of the HRC-S/HRMA is $\sim$1 arcsec. The measured detector QE at XRCF was found to be considerably lower than subassembly measurements made previously at SAO. Electronic modifications were made to the detector after the XRCF calibrations to restore the QE. Because of these changes, prediction of the on orbit effective area based on the XRCF calibrations will be complex. Flat field measurements that span the AXAF bandpass were made before and after the modifications, so that the XRCF calibrations can be transferred to the new flight configuration. The imaging capability of the detector was not changed by these modifications.

8 ACKNOWLEDGEMENTS

We are grateful for the support of Jack Gomes, Gerry Austin, John Polizotti, Richard Goddard, Frank DeFreze, Joseph D'Arco, Desi Hamvaz, and Frank Rivera. This work has been supported by NASA contract NAS8-38248.

9 REFERENCES

1. M. C. Weisskopf, S. L. O'Dell, R. F. Elsner, and L. P. Van Speybroeck, *X-ray and Extreme Ultraviolet Optics*, R. B. Hoover and A. B. C. Walker, Jr., eds., Proc. SPIE 2515, 1995.
2. A. C. Brinkman, J. J. van Rooijen, J. A. M. Bleeker, J. H. Dijkstra, J. Heise, P. A. J. de Korte, R. Mewe, and F. Paerels, *Astro. Lett. and Commun.*, 26, 1987.
3. C. R. Canizares, *et al.*, *Astro. Lett. and Commun.*, 26, 1987.
4. S. S. Murray, *et al.*, *Astro. Lett. and Commun.*, 26, 1987.
5. J. A. Nousek, *et al.*, *Astro. Lett. and Commun.*, 26, 1987.
6. R. Giaconni *et al.*, *Astrophysical Journal*, 230, 1979.
7. M. V. Zombeck, L. P. David, F. R. Harnden, Jr., and K. Kearns, *EUV, X-Ray, and Gamma-Ray Instrumentation for Astronomy VI*, O. H. W. Siegmund and J. V. Vallerga, eds., Proc. SPIE 2518, 1995.
8. R. P. Kraft, *et al.*, *EUV, X-Ray, and Gamma-Ray Instrumentation for Astronomy VII*, O. H. W. Siegmund and M. A. Gummin, eds., Proc. SPIE 2808, 1996.
9. K. A. Flanagan, M. Barbera, S. Murray, and M. Zombeck, *EUV, X-Ray and Gamma-Ray Instrumentation for Astronomy V*, O. H. W. Siegmund and J. V. Vallerga, eds., Proc. SPIE 2280, 1995.
10. A. T. Kenter, J. H. Chappell, R. P. Kraft, G. R. Meehan, S. S. Murray, and M. V. Zombeck, *EUV, X-Ray, and Gamma-Ray Instrumentation for Astronomy VII*, O. H. W. Siegmund and M. A. Gummin, eds., Proc. SPIE 2808, 1996.
11. G. R. Meehan, S. S. Murray, M. V. Zombeck, R. P. Kraft, K. Kobayashi, J. H. Chappell, A. T. Kenter, M. Barbera, A. Collura, and S. Serio, *these proceedings*.
12. G. R. Meehan, A. T. Kenter, R. P. Kraft, S. S. Murray, M. V. Zombeck, K. Kobayashi, J. H. Chappell, M. Barbera, and A. Collura, *EUV, X-Ray and Gamma-Ray Instrumentation for Astronomy VII*, O. H. W. Siegmund and M. A. Gummin, eds., Proc. SPIE 2808, 1996.
13. J. H. Chappell, R. K. Martin, S. S. Murray, and M. V. Zombeck, *X-ray and Gamma-Ray Instrumentation for Astronomy*, Proc. SPIE 1344, 1990.
14. J. H. Chappell, and S. S. Murray, *X-Ray Instrumentation in Astronomy and Atomic Physics*, Proc. SPIE 1159, 1989.
15. J. J. Drake, SAO Internal Memo, 1997.
16. S. S. Murray, *et al.*, *EUV, X-Ray, and Gamma-Ray Instrumentation in Astronomy, VIII*, O. H. W. Siegmund and M. A. Gummin, eds., Proc. SPIE, 3114, 1997.
17. S. E. Pearce, J. E. Lees, J. F. Pearson, G. W. Fraser, A. N. Brunton, K. A. Flanagan, A. T. Kenter, M. Barbera, V. Dhanak, A. Robinson, and D. Teehan, *EUV, X-Ray, and Gamma-Ray Instrumentation in Astronomy VI*, O. H. W. Siegmund and J. V. Vallerga, eds., Proc. SPIE 2518, 1995.
18. J. J. Kolodziejczak, R. A. Austin, R. F. Elsner, M. K. Joy, M. Sulkanen, E. M. Kellogg, and B. J. Wargelin, X-Ray and Extreme Ultraviolet Optics R. B. Hoover and A. B. Walker, eds., Proc SPIE 2515, 1995.
19. E. Y. Tsiang, R. J. Edgar, A. Tennant, S. A. Vitek, and E. M. Kellogg, *Grazing Incidence and Multilayer X-ray Optical Systems*, R. B. Hoover and A. B. C. Walker, eds., Proc SPIE, 3113, 1997.
20. P. Predehl, *et al.*, *Grazing Incidence and Multilayer X-ray Optical Systems*, R. B. Hoover and A. B. C. Walker, eds., Proc. SPIE 3113, 1997.
21. A. C. Brinkman, *et al.*, *Grazing Incidence and Multilayer X-ray Optical Systems*, R. B. Hoover and A. B. C. Walker, eds., Proc. SPIE 3113, 1997.